Journal of Advanced Ceramics
先进陶瓷
ISSN 2226-4108
CN 10-1154/TQ
清华大学出版社 Tsinghua University Press
SciOpen

J Adv Ceram 2026, **15**: 9221370

https://doi.org/10.26599/JAC.2026.9221370

Research Article

Achieving high piezoelectric response and elevated Curie temperature in Sm-modified PMN–PH–PT ceramics: A full-matrix characterization

Chunyang Gao[1], Ying Liu[2], Al Momin Md Tanveer Karim[1], Yue Luo[1], Zhenzhu Cao[1], Xiaozhou Liao[2], Zhenxiang Cheng[1], Shujun Zhang[1,3,*]

[1]*Institute for Superconducting and Electronic Materials, Australian Institute for Innovative Materials, University of Wollongong, Wollongong, Australia*

[2]*School of Aerospace, Mechanical and Mechatronic Engineering, and Australian Centre for Microscopy and Microanalysis, The University of Sydney, Sydney, Australia*

[3]*Department of Chemistry, City University of Hong Kong, Hong Kong, China*

*Corresponding author.

E-mail: s.j.zhang@cityu.edu.hk

Received: June 5, 2026; Revised: August 16, 2026; Accepted: September 3, 2026

清华大学出版社 Tsinghua University Press | SciOpen

Abstract: Pb-based ferroelectric ceramics face a fundamental trade-off between high piezoelectric response (d_{33}) and low Curie temperature (T_c). Here, we demonstrate that combining Sm-doping with a high-T_c $PbHfO_3$ (PH)-based ternary matrix can effectively shift this balance. A series of 0.01Sm-0.2PMN-(0.8−x)PH-xPT ceramics were designed and systematically characterized. A morphotropic phase boundary (MPB) was identified at $x \approx 0.435$, where the optimized composition exhibits a high d_{33} (≈ 830 pC/N) together with an elevated T_c (≈ 256 °C), a combination that lies above the typical d_{33}–T_c trend of Pb-based ferroelectric ceramics. In addition, the ceramic exhibits stable piezoelectric performance up to ~230 °C, indicating excellent thermal stability. A full-matrix electromechanical characterization was performed, yielding a self-consistent set of elastic, dielectric constants, and piezoelectric coefficients. Compared with a commercial PZT 610HD benchmark, the designed ceramic offers a comparable d_{33} but a 70 °C higher depolarization temperature. Atomic-resolution TEM reveals heterogeneous local polar configurations in the optimized composition, providing microscopic structural evidence consistent with its excellent piezoelectric performance. This comprehensive property set not only clarifies the intrinsic structure–property relations but also provides a reliable database for high-temperature piezoelectric device design.

Keywords: PMN-PH-PT, Sm doping, piezoelectricity, Full matrix, thermal stability

1 Introduction

Lead-based piezoelectric ceramics, particularly relaxor-$PbTiO_3$-based systems, are widely used in electromechanical devices due to their superior piezoelectric coefficients near the morphotropic phase boundary (MPB)[1-3]. However, further performance improvement is constrained by inherent trade-offs in material properties: a high piezoelectric coefficient often comes with a low Curie temperature (T_c), limiting the usable temperature range[4]. Modern applications, such as actuators and sensors in harsh environments, demand both high electromechanical response and stable operation up to elevated temperatures.

Various strategies have been explored to break this trade-off, among which rare-earth doping[5-7] has proven particularly effective in modifying local structural heterogeneity and polar nanoregions (PNRs), thereby facilitating polarization rotation and enhancing piezoelectric response. For example, Sm-doped $Pb(Mg_{1/3}Nb_{2/3})O_3$-$PbTiO_3$ (PMN-PT) ceramics exhibit ultrahigh piezoelectric coefficients (d_{33} up to ~1500 pC/N) together with extremely high dielectric constant [5]. However, their relatively low Curie temperature (~90 °C) severely restricts practical usage.

The multi-component solid-solution design[8-10] has also been leveraged, and more recently, high-entropy approach has emerged as an alternative strategy[11, 12]. By introducing increased configurational disorder and lattice distortion, high-entropy ceramics can achieve a flattened energy landscape and improved phase stability, resulting in enhanced dielectric properties and thermal stability[13, 14]. However, reports on significant enhancement of piezoelectric performance through high-entropy strategies remain limited, and the approach has so far shown greater success in improving stability than in boosting the piezoelectric response[15].

A more established and complementary approach is the introduction of a high-T_c third component into high-performance binary relaxor-PT systems. Ternary solid solutions such as

$PbZrO_3$ (PZ), $Pb(Yb_{1/2}Nb_{1/2})O_3$ (PYN), and $Pb(In_{1/2}Nb_{1/2})O_3$ (PIN) have been incorporated into PMN-PT to enhance thermal stability while retaining strong electromechanical response near the MPB[16-18]. For example, Sm-modified PMN-PZ-PT ceramics exhibit improved overall performance, with d_{33} up to ~745 pC/N and $T_c \approx 242$ °C at the MPB, together with stable piezoelectric and strain responses up to ~230 °C[19]. This suggests that combining rare-earth doping with a carefully selected high-T_c ternary matrix could offer a viable path toward simultaneously enhancing both piezoelectricity and thermal stability.

Owing to the chemical similarity between Zr and Hf, $PbHfO_3$ (PH) is often considered analogous to PZ in perovskite solid solutions. Both PH–PT and PZ–PT solid solutions form MPB compositions with relatively high Curie temperatures (~340 °C and ~385 °C, respectively)[20-22]. However, PH offers several potential advantages over PZ that motivate its selection here. First, the similar ionic size but significantly higher atomic mass of Hf^{4+} compared to Zr^{4+} may lead to different local lattice distortions and polarization dynamics, potentially enhancing domain contribution to piezoelectricity. Second, unmodified PMN-PH-PT ceramics have demonstrated a promising $d_{33} \approx 680$ pC/N and $T_c \approx 276$ °C, indicating that PH is indeed a suitable high-T_c end member for multicomponent design[18]. Nevertheless, rare-earth modification in this system remains largely unexplored, leaving a clear gap in understanding how Sm-doping might further optimize the d_{33}–T_c balance in this specific ternary matrix. Addressing this gap may provide an effective materials design strategy for simultaneously achieving high piezoelectric performance and elevated operating temperature in Pb-based piezoceramics.

Based on the preliminary composition screening, the Sm concentration was fixed at 1 mol%, and the present work systematically investigates the effect of PT content on the phase evolution and electromechanical properties of Sm-modified PMN–PH–PT ceramics. The specific aims are threefold: (i) to establish the composition-dependent phase evolution and locate the MPB;

(ii) to evaluate the dielectric, ferroelectric, piezoelectric, and high-field strain responses, with emphasis on the d_{33}–T_c balance and its thermal stability; and (iii) to perform a full-matrix electromechanical characterization according to IEEE Standard on Piezoelectricity[23] that yields a complete, self-consistent set of material constants. By benchmarking against a commercial soft PZT5H ceramic (PZT-610HD, TRS Technologies, USA), we highlight the advantages of the present system for high-temperature piezoelectric applications. Unlike previous Pb-based studies that primarily focused on transparency, strain optimization, or individual functional properties, the present work combines composition optimization with comprehensive IEEE-standard full-matrix characterization, providing a more complete evaluation of the electromechanical performance for application-oriented material design [24-26].

2 Experimental procedures

2.1 Sample Preparation and Characterization

1 mol% Sm-doped 0.2PMN-(0.8−x)PH-xPT ceramics (denoted as 0.01Sm-0.2PMN-(0.8−x)PH-xPT) were prepared by a precursor-assisted solid-state reaction method using high-purity PbO (99.95%), Sm_2O_3 (99.9%), $MgNb_2O_6$ (99.99%), HfO_2 (99.9%), and TiO_2(99.8%) powders. The powders were ball-milled in ethanol for 12-24 h, dried, and calcined at 850 °C for 4 h. After re-milling, the powders were pressed into pellets (~12-15 mm in diameter) under ~200 MPa. Binder burnout was carried out at 600 °C for 2h, followed by sintering at 1250 °C for 2 h in a PbO-rich atmosphere. Post-sintering annealing was performed at 1050 °C for 5 h. The sintered samples were polished, cleaned, and electroded with silver paste (DuPont 6160, DuPont, USA). Electrical poling was conducted in silicone oil at 100 °C under a DC field of ~30 kV/cm for 10 min.

The phase structure was characterized by X-ray diffraction (XRD, Aeris, Malvern Panalytical, The Netherlands) using Cu–Kα radiation. Rietveld refinement was further

performed using a two-phase structural model consisting of rhombohedral *R3m* and tetragonal *P4mm* phases, with detailed refinement results provided in the Supporting Information. The microstructure of selected samples was examined by scanning electron microscopy (SEM, JSM-7500FA, JEOL, Japan). Transmission electron microscopy (TEM) bright-field images, selected-area electron diffraction (SAED) patterns, and high-resolution scanning TEM (STEM) high-angle annular dark-field (HAADF) images were acquired using a Thermo Fisher Themis-Z Double-corrected 60–300 kV scanning/transmission electron microscope (S/TEM). The convergence and collection angles under the STEM–HAADF mode are 17.9 and 50–200 mrad, respectively. The point resolution of Themis-Z under the STEM mode is around 0.6 Å (operated at 300 kV). A Python library "Atomap" was used to extract atom positions from atomic-resolution STEM–HAADF images by fitting 2D Gaussian functions to every atomic column. The extracted atomic positions were employed to determine projected Pb-site displacements with respect to their four nearest B-site ions. Dielectric properties were measured as a function of temperature and frequency using an LCR meter (4980AL, Keysight Technologies, USA) in a computer-controlled furnace over a frequency range of 1-100 kHz with a heating rate of 2 °C/min, from which the T_c was determined.

Ferroelectric polarization–electric field (*P*-*E*) loops and strain-electric field (*S*-*E*) behavior were measured using a ferroelectric test system (TFA2000, aixACCT Systems, Germany). The high-field piezoelectric coefficient d_{33}^* was obtained from the slope of the unipolar *S*-*E* curves. The piezoelectric coefficient d_{33} was measured using a Berlincourt-type meter (ZJ-3A, China). The temperature dependence of d_{33} was evaluated using both in-situ and ex-situ methods. For in-situ measurements, d_{33} was recorded during heating, whereas for ex-situ measurements, samples were annealed at selected temperatures under short-circuit conditions for 30 min prior to measurement at room temperature.

2.2 Full-matrix characterization

Full-matrix electromechanical characterization was performed using the resonance-antiresonance method under small-signal conditions. Prior to impedance measurements, the specimens were prepared from sintered pellets (~15 mm in diameter) and machined into geometries appropriate for different vibration modes using a precision diamond saw. Custom alignment fixtures were employed during machining to ensure accurate geometrical control, including parallelism and perpendicularity of the specimen surfaces.

All specimens for impedance measurements were coated with gold electrodes using a rotary target plasma sputtering coater (VTC-16-3HD, MTI, USA). Poling directions were configured according to the required vibration modes. For shear-mode specimens, additional electrode reconfiguration was applied to achieve the appropriate poling orientation.

Impedance spectra were recorded using an impedance analyzer (HP 4294A, Agilent Technologies, USA), and the resonance (f_r) and anti-resonance (f_a) frequencies were identified from the impedance magnitude and phase responses.

Five principal vibration modes were measured, including planar (radial), thickness extensional, longitudinal, transverse length-extensional, and thickness-shear modes. The planar and thickness extensional modes were measured using disk specimens and were used to determine k_p, k_t, and c_{33}^D. Longitudinal-mode specimens were used to obtain k_{33} and s_{33}^D, while transverse length-extensional specimens provided k_{31} and s_{11}^E. Thickness-shear specimens were used to determine k_{15} and c_{44}^D. These measured quantities, together with dielectric permittivities measured along the longitudinal and transverse directions, were used to calculate the complete set of elastic, dielectric, and piezoelectric constants assuming macroscopic 6mm symmetry.

Only well-defined resonance modes with clearly resolved f_r and f_a and minimal mode coupling were selected for parameter extraction. When possible, at least three specimens were

measured for each vibration mode to verify reproducibility. The extracted constants were further checked using internal consistency relations among coupling factors, dielectric constants, and resonance-derived parameters. Detailed equations and calculation procedures are provided in the Supporting Information.

3 Results and discussions

3.1 Phase Structure

Fig. 1 presents the X-ray diffraction (XRD) patterns of 0.01Sm-0.2PMN-(0.8−*x*)PH-*x*PT ceramics, together with enlarged views of the pseudocubic (200) reflections, which are commonly used to identify phase evolution across the MPB in Pb-based perovskite ceramics. All compositions exhibit a single-phase perovskite structure without detectable secondary phases, indicating the successful incorporation of Sm^{3+} ions into the lattice.

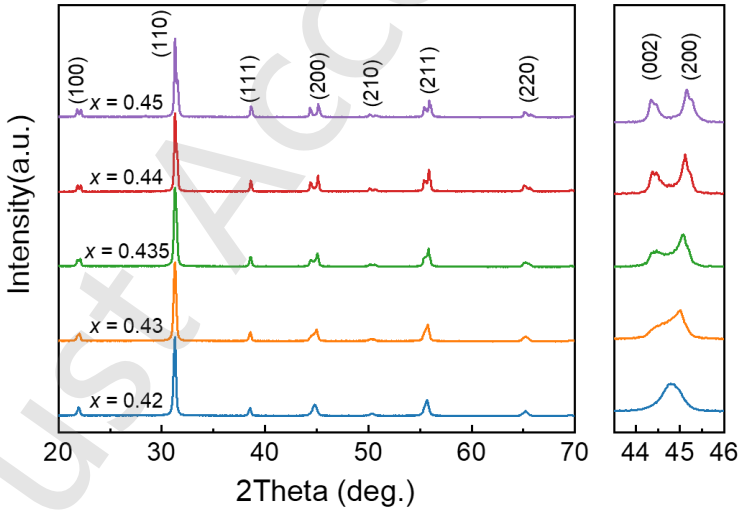

Fig. 1 XRD patterns of 0.01Sm-0.2PMN-(0.8−*x*)PH-*x*PT ceramics with varying PT content and enlarged pseudocubic (200) reflections.

With increasing PT content, a systematic evolution of the crystal structure is observed. At lower PT content, the (200) reflection appears as a nearly symmetric single peak, characteristic of a rhombohedral-dominated phase. As the PT content increases, the peak gradually broadens, suggesting the onset of phase coexistence. A further increase in PT content leads to a clear splitting of the (200) reflection into (200)/(002) peaks, indicating the development of a

tetragonal phase. A similar evolution from a single peak to split peaks is also observed for the (100), (210), and (211) reflections, providing additional evidence for the rhombohedral-to-tetragonal phase transition. This evolution implies the formation of a morphotropic phase boundary at intermediate compositions, which is generally associated with enhanced dielectric and piezoelectric properties [27, 28].

To further quantify the phase evolution, Rietveld refinement was performed using an *R3m* + *P4mm* two-phase model (Figure S5 and Table S3). The tetragonal phase fraction increases progressively from approximately 41.0% at $x = 0.42$ to 92.3% at $x = 0.45$, accompanied by an increase in the tetragonal c/a ratio from 1.0082 to 1.0164. These results confirm the gradual evolution from a rhombohedral-rich to a tetragonal-rich structure with increasing PT content and support the phase coexistence in the MPB region.

3.2 Dielectric, Ferroelectric, and Piezoelectric Properties

The composition-dependent dielectric, ferroelectric and piezoelectric properties of 0.01Sm-0.2PMN-(0.8−*x*)PH-*x*PT ceramics are summarized in Fig. 2 and Table 1. All compositions exhibit a pronounced dielectric maximum corresponding to the ferroelectric–paraelectric phase transition, as shown in Fig. 2(a). The T_c increases gradually with increasing PT content, from 251 °C at $x = 0.42$ to 263 °C at $x = 0.45$, due to the fact that PT end member possesses a higher Curie temperature, which is expected to benefit the thermal stability.

The room-temperature dielectric constant shows a strong composition dependence. As summarized in Fig. 2(c), ε_r increases significantly from 1070 at $x = 0.42$ to a maximum value of 3500 at $x = 0.435$, followed by a decrease to 2560 at $x = 0.45$. This pronounced enhancement in dielectric constant is consistent with the structural evolution identified by XRD, where phase coexistence at MPB region facilitates polarization rotation and increases the dielectric response.

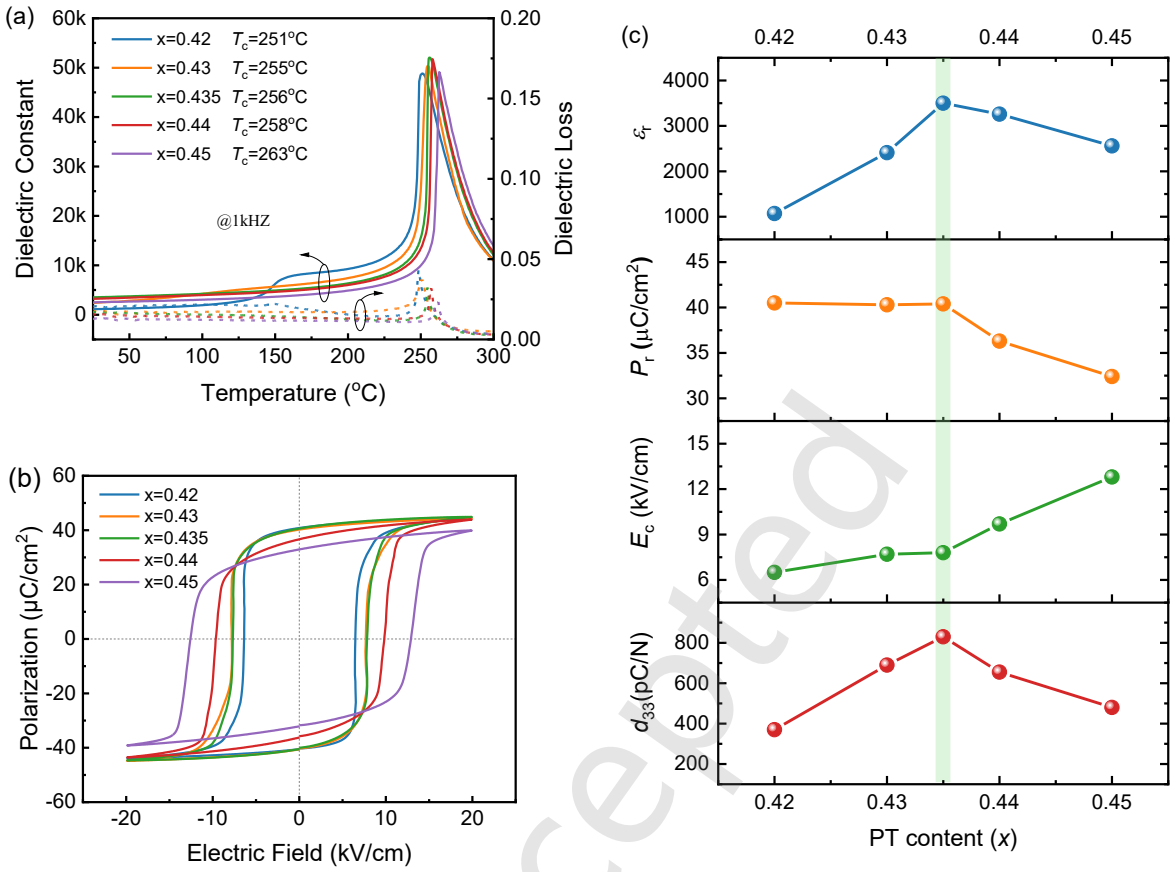

Fig. 2 (a) Temperature dependence of dielectric permittivity (ε_r) and dielectric loss (*tanδ*) at 1 kHz for 0.01Sm-0.2PMN-(0.8−*x*)PH-*x*PT ceramics. (b) Polarization–electric field (*P*–*E*) hysteresis loops at 1 kHz for different compositions. (c) Composition dependence of dielectric permittivity, remnant polarization P_r, coercive field E_c, and piezoelectric coefficient d_{33}.

Table 1 Dielectric, Ferroelectric, and Piezoelectric Properties of 0.01Sm-0.2PMN-(0.8−*x*)PH-*x*PT Ceramics.

Composition	**ε_r**	**tan δ**	**T_c (°C)**	**P_r (μC/cm²)**	**E_c (kV/cm)**	**d_{33} (pC/N)**	**d_{33}^* (pm/V)**
x=0.42	1070	0.018	251	40.5	6.5	370	730
x=0.43	2410	0.016	255	40.3	7.7	690	810
x=0.435	3500	0.017	256	40.5	7.8	830	840
x=0.44	3260	0.014	258	36.3	9.7	655	870
x=0.45	2560	0.013	263	32.4	12.8	480	680

The ferroelectric properties are presented in Fig. 2(b). All compositions exhibit well-saturated *P*–*E* hysteresis loops, indicating typical ferroelectric behavior. The remnant

polarization (P_r) remains relatively stable in the composition range of x = 0.42-0.435, with values around 40.3-40.5 μC/cm², and then decreases with further increasing PT content, reaching 36.3 μC/cm² at x = 0.44 and 32.4 μC/cm² at x = 0.45. In contrast, the coercive field (E_c) increases continuously from 6.5 kV/cm to 12.8 kV/cm over the same composition range, indicating that domain switching becomes progressively more difficult in the tetragonal-rich region[29]. This behavior may be associated with the increased lattice distortion of the tetragonal phase, as evidenced by the progressively increasing c/a ratio obtained from Rietveld refinement (Table S3).

The composition dependence of the piezoelectric coefficient d_{33} is also shown in Fig. 2(c), following a similar trend: it increases from 370 pC/N at x = 0.42 to a maximum of 830 pC/N at x = 0.435, and then declines at higher PT contents. Taken together, the composition-dependent evolution of dielectric, ferroelectric, and piezoelectric properties strongly suggests that the MPB region is located at x = 0.435, in good agreement with the observation of the phase/structure evolution with composition, providing an optimal balance of functional performance.

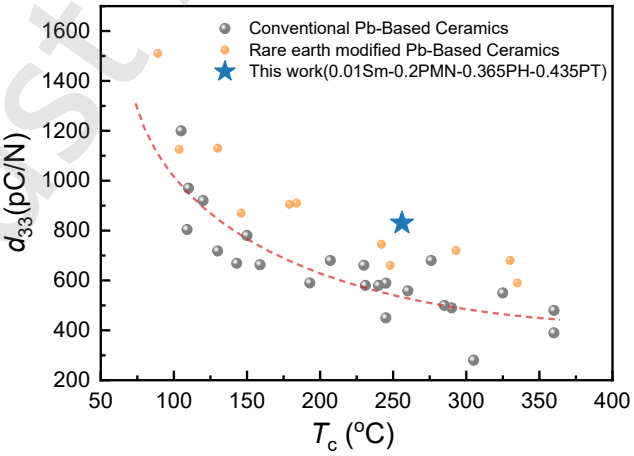

Fig. 3 Relationship between piezoelectric coefficient d_{33} and Curie temperature T_c for representative Pb-based piezoelectric ceramics compiled from literature data. The dashed line indicates the general trade-off trend between d_{33} and T_c. The present composition is highlighted.

Notably, when comparing the d_{33}–T_c trade-off with previously reported Pb-based ferroelectric solid solutions, as illustrated in Fig. 3[6, 7, 17, 19, 24, 25, 30-34], the present composition ($d_{33} \approx 830$ pC/N, $T_c \approx 256$ °C) lies above the general trend, demonstrating a competitive combination of high piezoelectric response and elevated Curie temperature.

3.3 Atomic-scale Structural Characterization

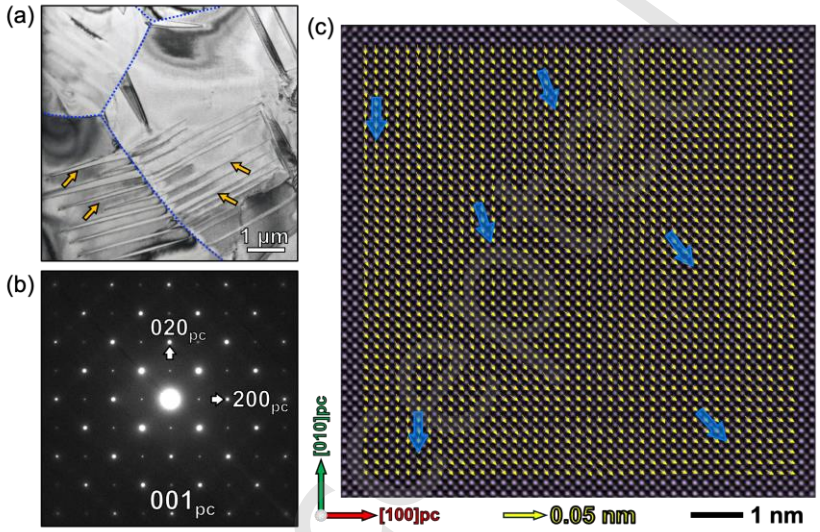

Fig. 4 TEM characterization of the optimized 0.01Sm–0.2PMN–0.365PH–0.435PT ceramic. (a) Bright-field TEM image showing domain contrast (indicated by yellow arrows). Grain boundaries are traced by blue dotted lines. (b) Selected-area electron diffraction (SAED) pattern indexed along the [001]pc zone axis. (c) Atomic-resolution HAADF-STEM image with projected Pb displacement vectors, revealing locally heterogeneous polar configurations.

Transmission electron microscopy (TEM) was performed to further investigate the local structural characteristics of the optimized 0.01Sm–0.2PMN–0.365PH–0.435PT ceramic. As shown in Fig. 4(a), well-developed lamellar ferroelectric domains are observed within the grains. The corresponding selected-area electron diffraction (SAED) pattern (Fig. 4(b)), indexed along the pseudocubic [001] zone axis, exhibits a well-defined perovskite diffraction pattern without obvious extra reflections, consistent with the average crystal structure identified by XRD.

To further examine the local polar structure, high-angle annular dark-field scanning transmission electron microscopy (HAADF-STEM) was performed along the pseudocubic [001] direction. As shown in Fig. 4(c), the projected Pb-displacement vectors exhibit pronounced spatial correlations, with their orientations varying between the projected ⟨100⟩- and ⟨110⟩-type directions, corresponding to tetragonal-like and rhombohedral-/orthorhombic-like local polar configurations, respectively[35]. The gradual spatial variation of the displacement orientations over several nanometres indicates the presence of heterogeneous local polar configurations[36].

Such heterogeneous local polar configurations have been widely reported to facilitate polarization reorientation under an applied electric field by flattening the free-energy landscape, thereby contributing to enhanced electromechanical responses in relaxor ferroelectrics[5, 31, 37]. The local polar heterogeneity observed here therefore provides microscopic structural evidence that is consistent with the excellent piezoelectric performance of the optimized Sm-modified PMN–PH–PT ceramic.

3.4 Strain Behavior Under High Electric Field

The strain behavior of the ceramics under high electric fields was systematically investigated using unipolar strain–electric field (*S*-*E*) measurements. The high-field piezoelectric coefficient (d_{33}^*) and strain hysteresis (*H*) were extracted to evaluate the electromechanical response. *H* reflects the energy loss during electric-field cycling, which is mainly associated with the irreversible motion of domain walls[38]. The high-field piezoelectric coefficient is defined as $d_{33}^*=S_{max}/E_{max}$, where S_{max} and E_{max} are the maximum strain and applied electric field, respectively. The strain hysteresis is evaluated from the difference between the increasing and decreasing branches of the *S*–*E* curve at half of the maximum electric field, normalized to the maximum strain[39].

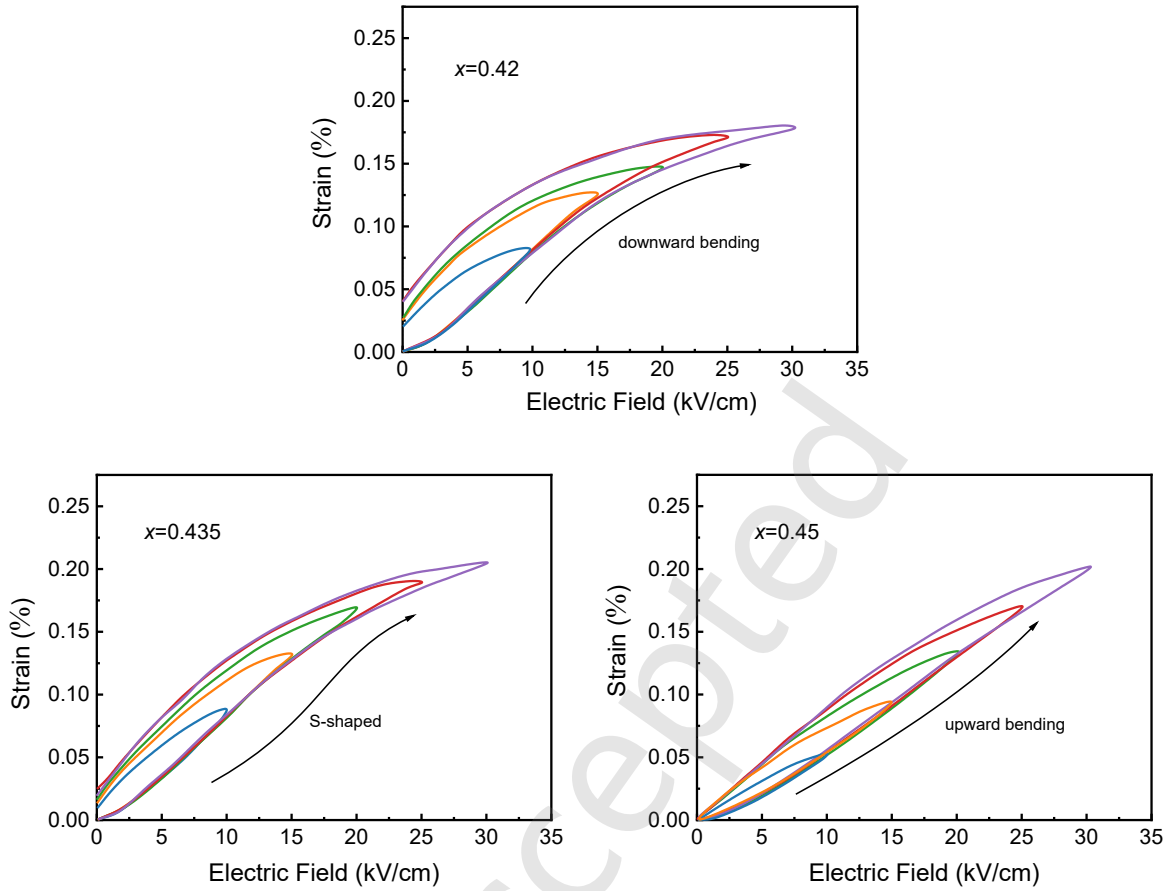

Fig. 5 Unipolar strain–electric field (*S*–*E*) responses of 0.01Sm-0.2PMN-(0.8−*x*)PH-*x*PT ceramics with x = 0.42, 0.435 and 0.45 under varying electric fields at 1 Hz.

The high-field strain response of the ceramics is presented in Fig. 5. Three representative compositions, x = 0.42, 0.435, and 0.45, were selected to correspond to rhombohedral-rich (R), MPB, and tetragonal-rich (T) regions, respectively, based on the phase structure analysis.

Distinct differences in the shape of the *S*–*E* curves are observed for the three compositions. The x = 0.42 composition exhibits a downward-bending strain response at high electric fields, indicating a reduction in incremental strain at elevated fields. The x = 0.435 composition shows a S-shaped behavior, characterized by an increase at low to intermediate electric fields followed by a slight deviation at higher fields. In contrast, the x = 0.45 composition displays a slightly upward-bending strain response, reflecting a comparatively weak field dependence. These differences in strain evolution suggest distinct domain-switching behaviors associated with the

R, MPB, and T regions, which have been widely discussed in $PbTiO_3$-based systems[22, 26, 39].

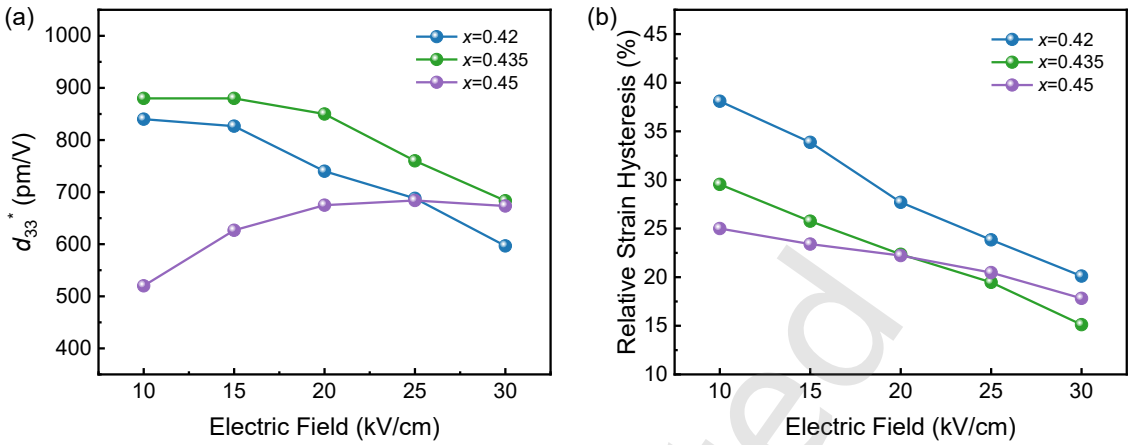

Fig. 6 (a) High-field piezoelectric coefficient (d_{33}^*) and (b) relative strain hysteresis as a function of electric field for 0.01Sm-0.2PMN-(0.8−x)PH-xPT ceramics with x = 0.42, 0.435, and 0.45.

To further quantify the electromechanical response, the high-field piezoelectric coefficient d_{33}^* was calculated and is presented in Fig. 6(a). For the x = 0.42 and x = 0.435 compositions, d_{33}^* decreases progressively with increasing electric field, gradually approaching a linear decline at higher fields. In contrast, the x = 0.45 composition exhibits an initial increase in d_{33}^*, followed by a more gradual stabilization at higher fields. Notably, the x = 0.435 composition exhibits the highest d_{33}^* values over the low-to-intermediate electric field range, which is characteristic of compositions near the MPB, where the coexistence of rhombohedral and tetragonal phases facilitates domain switching and leads to enhanced electromechanical response[39].

The field dependence of d_{33}^* can be understood in terms of the combined contributions of intrinsic lattice response and extrinsic domain wall motion[40]. At relatively low electric fields, non-180° domain switching contributes significantly to the strain response, particularly for compositions near the MPB. With increasing electric field, domains progressively align along the field direction, and further contributions from domain switching become increasingly limited due to domain alignment and clamping effects, leading to a reduction in d_{33}^*[1, 37].

The relative strain hysteresis as a function of electric field is shown in Fig. 6(b). For all compositions, the hysteresis decreases monotonically with increasing electric field, indicating a gradual reduction of irreversible domain switching at higher fields. The x = 0.42 and x = 0.435 compositions exhibit similar decreasing trends, while the x = 0.45 composition shows a more gradual reduction over the entire field range. The x = 0.42 composition exhibits relatively higher hysteresis values, which can be associated with a relatively larger contribution from irreversible domain-wall motion in the rhombohedral-rich region[22].

The combined evolution of d_{33}^* and hysteresis further reflects the domain-switching characteristics across different phase regions. For both the rhombohedral-rich (x = 0.42) and MPB (x = 0.435) compositions, the similar decreasing trends of d_{33}^* and hysteresis with increasing electric field are consistent with the progressive reduction of effective domain switching contribution at higher fields. In particular, the relatively small variation of d_{33}^* in the MPB composition at low-to-intermediate electric fields indicates that the electromechanical response is maintained over a relatively wide field range.

In contrast, the tetragonal-rich composition (x = 0.45) exhibits an initial increase in d_{33}^*, followed by a more gradual variation at higher fields, together with a more gradual decrease in hysteresis. This behavior may be associated with the increased lattice distortion in the tetragonal-rich region, consistent with the higher c/a ratio obtained from Rietveld refinement (Table S3), which can constrain domain reorientation and domain-wall motion[41]. As a result, domain switching becomes more difficult to activate at low electric fields, with the effective activation of domain-wall motion being delayed, limiting the contribution from extrinsic strain mechanisms and leading to a more stable electromechanical response, which can be maintained at high electric fields.

3.5 Thermal stability of piezoelectric properties

The thermal stability of the piezoelectric response was evaluated using both in-situ temperature-dependent d_{33} measurements and ex-situ characterization, as shown in Fig. 7**.** In the in-situ measurements, d_{33} was recorded directly as a function of temperature, whereas the ex-situ d_{33} was measured at room temperature after short-circuit annealing at respective high temperatures to evaluate the irreversible depolarization. This combined approach enables a clear distinction between the reversible temperature response and depolarization behavior.

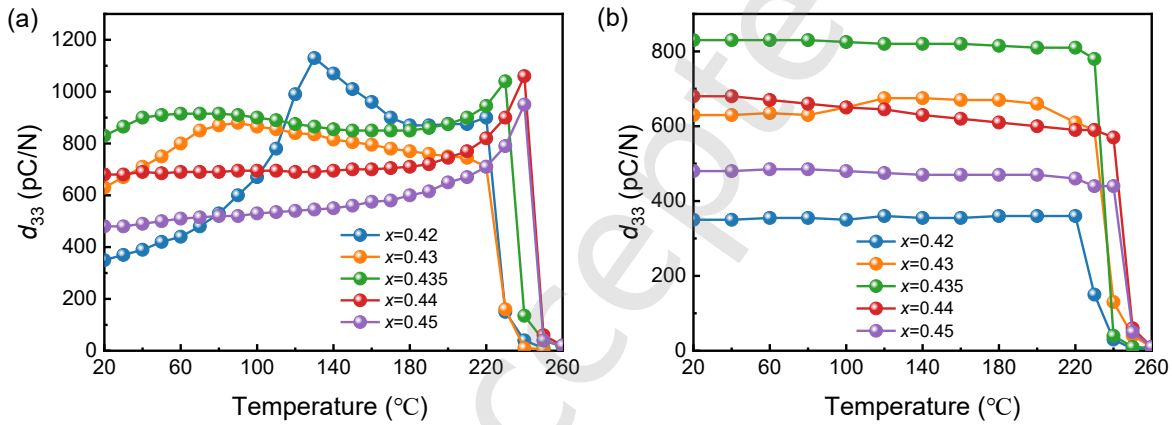

Fig. 7 The temperature dependence of (a) in-situ d_{33} and (b) ex-situ d_{33} for 0.01Sm-0.2PMN-(0.8–*x*)PH-*x*PT ceramics.

As shown in Fig. 7(a), the in-situ d_{33} exhibits strongly composition-dependent temperature evolution. For the compositions on the lower-PT side of the MPB (x = 0.42 and 0.43), d_{33} initially increases with temperature, reaches a pronounced maximum, and subsequently decreases upon further heating. This peak-like behavior is indicative of temperature-induced phase instability, which is commonly associated with a transition toward the tetragonal phase, leading to a temporary enhancement of the piezoelectric response at intermediate temperatures corresponding to their respective rhombohedral to tetragonal phase transitions [42]. Similar behavior has been reported in related Sm-modified PMN-PZ-PT systems[17].

In contrast, the MPB composition (x = 0.435) exhibits the most stable d_{33} response over a broad temperature range prior to depolarization, with minimal variation at intermediate

temperatures. Both the in-situ and ex-situ results consistently indicate that this composition maintains a relatively high d_{33} up to elevated temperature (≈230 °C), demonstrating superior thermal stability compared to the other compositions. The tetragonal-side compositions (x = 0.44 and 0.45) exhibit a relatively weak temperature dependence at lower temperatures, followed by a more pronounced increase in d_{33} immediately prior to depolarization. This increase, commonly observed in temperature-dependent piezoelectric measurements, may be associated with thermally activated domain response as the system approaches depolarization.

The onset of depolarization is more clearly revealed by the ex-situ measurements shown in Fig. 7(b). For all compositions, the room-temperature d_{33} remains nearly constant up to a critical annealing temperature, followed by a sharp decrease, indicating the loss of macroscopic polarization. The depolarization temperatures identified from the ex-situ measurements are in good agreement with the abrupt drop observed in the in-situ d_{33} curves.

3.6 Benchmark and Full-Matrix Electromechanical Characterization

To achieve a comprehensive and internally consistent evaluation of electromechanical behavior, full-matrix characterization based on IEEE standard was employed. The composition with x = 0.435, identified as the optimized composition in this work (hereafter referred to as the Sm-doped ceramic, SDC), was selected for detailed investigation.

To benchmark the performance and validate the reliability of the measurements, a commercial soft PZT5H ceramic (PZT-610HD, TRS Technologies, USA), known for its high piezoelectric performance, was investigated under identical experimental conditions. All samples were prepared with comparable geometries and tested using the same procedures to ensure consistent boundary conditions, and the measured results for PZT-610HD were further compared with manufacturer-reported datasheet values.

3.6.1 Benchmark and Basic Properties

To establish a baseline for comparison prior to full-matrix analysis, the basic electromechanical properties of the Sm-doped ceramic (SDC) were re-examined in comparison with the commercial PZT-610HD.

As summarized in Table 2, both materials exhibit similarly high piezoelectric coefficients, indicating comparable room-temperature electromechanical performance. However, the SDC shows a significantly higher Curie temperature, increased by approximately 46 °C compared to PZT-610HD, suggesting improved thermal stability while maintaining a high piezoelectric response. The dielectric constant and loss are slightly lower than those of PZT-610HD, while other ferroelectric parameters remain broadly comparable, with a slightly higher remnant polarization and a similar coercive field observed for the SDC.

Table 2. Summary of main properties of SDC and PZT 610HD.

Sample	ε_r	**tan δ**	T_c **(°C)**	T_d **(°C)**	d_{33} **(pC/N)**	P_r **(μC/cm²)**	E_c **(kV/cm)**
SDC	3530	0.017	256	230	830	40.5	7.8
PZT 610HD	4100	0.027	210	160	850	35.4	7.7

The temperature dependence of the piezoelectric coefficient is further compared in Fig. 8, where the depolarization temperature (T_d) is identified from both in-situ and ex-situ measurements with good agreement. For PZT-610HD, a rapid degradation of d_{33} is observed at approximately 160 °C, well below its Curie temperature, indicating a relatively large separation between T_d and T_c. In contrast, the SDC maintains its piezoelectric response up to a much higher depolarization temperature of approximately 230 °C, about 70 °C higher than that of PZT-610HD. This corresponds to approximately 0.9 T_c of the SDC, indicating that depolarization occurs in much closer proximity to the Curie temperature than typically observed in conventional piezoelectric ceramics.

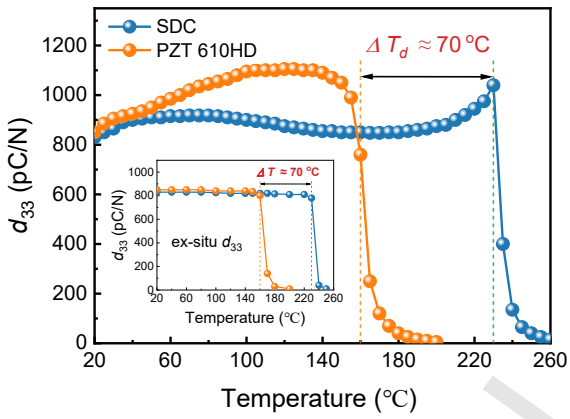

Fig. 8 Temperature dependence of in-situ d_{33} for SDC and PZT-610HD ceramics. Insets show the ex-situ d_{33}.

In addition to the higher depolarization temperature, the SDC also exhibits a much smaller variation in d_{33} before depolarization. Compared with PZT-610HD, which shows a pronounced temperature-dependent change prior to its rapid degradation, the SDC maintains a more temperature-insensitive piezoelectric response over a broader temperature range. This combination of higher T_d and reduced d_{33} variation indicates a wider and more stable operating temperature window.

3.6.2 Full matrix electromechanical constants

Prior to full-matrix analysis, the microstructure and bulk density of the ceramics were evaluated. The SEM microstructures (Fig. S4) reveal dense ceramics with grain sizes of ~2.6 μm for SDC and ~3.8 μm for PZT-610HD. Although the SDC exhibits a slightly smaller average grain size, the two ceramics remain broadly comparable in microstructure, suggesting that microstructural differences are unlikely to dominate the subsequent comparison of electromechanical properties. The bulk densities are 8.75 g/cm^3 for the SDC and 7.95 g/cm^3 for PZT-610HD, providing a reliable basis for subsequent parameter extraction.

While conventional characterization is typically based on a limited number of parameters such as d_{33} and k_p, practical piezoelectric device design requires a complete set of

electromechanical, dielectric, and elastic constants to accurately describe material behaviour under different vibration modes and electrical boundary conditions. The full-matrix characterization presented here therefore provides a more comprehensive evaluation of the optimized SDC. Combined with the benchmark comparison against commercial PZT-610HD, it enables a direct assessment of the potential of this material for high-temperature piezoelectric transducers and actuators.

The full set of electromechanical constants of the SDC and PZT-610HD ceramics, determined based on IEEE Standard on Piezoelectricity, is summarized in Table 3. For PZT-610HD, both the measured values and the manufacturer-provided datasheet values are included for comparison. The good agreement between the measured and datasheet values confirms the reliability of the experimental measurements and indicates that the extracted constants provide a physically meaningful and self-consistent description of the material behavior.

Table 3 Full-Matrix Electromechanical Constants of SDC and PZT-610HD (Measured vs Datasheet Values).

Category	Parameter	SDC	PZT-610HD (Measured)	PZT-610HD (Datasheet)
Coupling	k_p	75.1%	72.5%	74.9%
	k_t	53.7%	56.5%	56.0%
	k_{33}	80.7%	79.8%	80.2%
	k_{31}	-44.2%	-43.7%	-46.9%
	k_{15}	75.9%	75.5%	76.0%
Elastic	s_{11}^E (10^{-12} m^2/N)	16.4	15.2	16.5
	s_{12}^E (10^{-12} m^2/N)	-5.0	-4.2	-3.6
	s_{13}^E (10^{-12} m^2/N)	-8.8	-8.5	-9.5
	s_{33}^E (10^{-12} m^2/N)	22.4	21.5	22.1
	s_{44}^E (10^{-12} m^2/N)	45.4	48.5	48.0
	s_{66}^E (10^{-12} m^2/N)	42.9	38.7	40.1
	s_{11}^D (10^{-12} m^2/N)	13.2	12.3	12.9
	s_{12}^D (10^{-12} m^2/N)	-8.2	-7.1	-7.2
	s_{13}^D (10^{-12} m^2/N)	-2.0	-2.2	-2.4

	s_{33}^D (10^{-12} m^2/N)	7.8	7.8	7.9
	s_{44}^D (10^{-12} m^2/N)	19.2	20.8	20.3
	s_{66}^D (10^{-12} m^2/N)	42.9	38.7	40.1
	c_{11}^E (10^{10} N/m^2)	13.6	14.1	13.2
	c_{12}^E (10^{10} N/m^2)	8.9	8.9	8.2
	c_{13}^E (10^{10} N/m^2)	8.8	9.1	9.2
	c_{33}^E (10^{10} N/m^2)	11.4	11.4	11.6
	c_{44}^E (10^{10} N/m^2)	2.2	2.1	2.1
	c_{66}^E (10^{10} N/m^2)	2.3	2.6	2.5
	c_{11}^D (10^{10} N/m^2)	14.9	15.1	14.3
	c_{12}^D (10^{10} N/m^2)	10.2	9.9	9.3
	c_{13}^D (10^{10} N/m^2)	6.4	7.2	7.5
	c_{33}^D (10^{10} N/m^2)	16.0	16.8	16.9
	c_{44}^D (10^{10} N/m^2)	5.2	4.8	4.9
	c_{66}^D (10^{10} N/m^2)	2.3	2.6	2.5
Piezoelectric	d_{33} (pC/N)	675	705	737
	d_{31} (pC/N)	-316	-325	-373
	d_{15} (pC/N)	850	930	981
	e_{33} (C/m^2)	20.9	21.1	16.9
	e_{31} (C/m^2)	-11.5	-10.6	-11.6
	e_{15} (C/m^2)	18.7	19.2	20.4
	g_{33} (10^{-3} Vm/N)	21.6	19.4	19.3
	g_{31} (10^{-3} Vm/N)	-10.1	-8.9	-9.7
	g_{15} (10^{-3} Vm/N)	30.9	29.6	28.3
	h_{33} (10^8 V/m)	21.3	17.9	14.7
	h_{31} (10^8 V/m)	-11.7	-9.0	-10.0
	h_{15} (10^8 V/m)	16.9	15.6	14.0
Dielectric	$\varepsilon_{33}^T / \varepsilon_0$	3530	4100	4320
	$\varepsilon_{11}^T / \varepsilon_0$	3100	3550	3920
	$\varepsilon_{33}^S / \varepsilon_0$	1110	1330	1300
	$\varepsilon_{11}^S / \varepsilon_0$	1250	1390	1650
	$\beta_{33}^T \cdot \varepsilon_0$ (10^{-4})	2.8	2.4	2.3
	$\beta_{11}^T \cdot \varepsilon_0$ (10^{-4})	3.2	2.8	2.6
	$\beta_{33}^S \cdot \varepsilon_0$ (10^{-4})	9.0	7.5	7.7
	$\beta_{11}^S \cdot \varepsilon_0$ (10^{-4})	8.0	7.2	6.1

The electromechanical coupling factors of the SDC ceramic are generally comparable to those of PZT-610HD across multiple vibration modes. In particular, the k_{33} and k_{15} values remain at similarly high levels, indicating efficient electromechanical energy conversion in both longitudinal and shear modes. The k_p and k_{31} values also fall within a comparable range, while the elastic and dielectric constants exhibit consistent trends without abnormal deviations.

The piezoelectric coefficients derived from the full-matrix analysis further support this observation. Although the d_{33} value of the SDC (≈675 pC/N) is moderately lower than that of PZT-610HD (≈705 pC/N) under small-signal conditions, it remains at a high level, while the shear-related coefficient d_{15} also maintains strong piezoelectric activity, with values of ≈850 pC/N for SDC compared to ≈930 pC/N for PZT-610HD. These results indicate that the SDC preserves effective electromechanical coupling across multiple modes, providing a physically consistent description of its behavior.

To further assess the reliability of the extracted full-matrix constants, the internal consistency between directly measured and derived parameters was examined, as summarized in Table 4. For both SDC and PZT-610HD, the coupling factors calculated from different approaches show good agreement with the directly measured values, with deviations typically within ~2-3%. This self-consistency confirms that the extracted constants form a physically reliable and complete description of SDC.

A larger discrepancy is observed for d_{33}, where the values derived from the full-matrix constants are lower than the quasi-static values by approximately 17–18%. This difference is attributed to the distinction between small-signal resonance measurements and quasi-static measurements, the latter including additional extrinsic contributions such as domain-wall motion. Similar differences between resonance-derived and quasi-static values have also been reported in full-matrix studies of piezoelectric ceramics[43]. In comparison, the high-field piezoelectric coefficient d_{33}^* remains at a similarly high level for both materials, indicating

strong electromechanical response under large-signal conditions (see Section 3.4). Overall, the agreement among parameters derived from different modes and methods confirms the physical reliability of the extracted full-matrix constants.

Table 4 Comparison of electromechanical parameters derived from different methods for SDC and PZT-610HD.

Parameter	Method	SDC	PZT-610HD	Deviation (SDC)	Deviation (PZT)
k_{33}	Measured (resonance)	80.7%	79.8%	-	-
	Calculated (ε^t, ε^s)	82.8%	82%	~2.6%	~2.8%
	From kp, kt relation	83%	82%	~2.9%	~2.8%
k_{15}	Measured (resonance)	75.9%	75.5%	-	-
	Calculated (ε^t, ε^s)	77%	78%	~1.5%	~3.3%
d_{33} (pC/N)	Measured (meter)	830	850	-	-
	Calculated (full-matrix)	675	705	~18.7%	~17.2%
d_{33}^* (pm/V)		840	870	-	-

4 Conclusions

This work demonstrates that a rational combination of Sm-doping and a high-T_c $PbHfO_3$-based ternary matrix effectively mitigates the classical d_{33}–T_c trade-off in lead-based piezoceramics. By systematically varying the PT content in 0.01Sm-0.2PMN-(0.8−x)PH-xPT ceramics, we identified the MPB around $x = 0.435$, within the gradual structural evolution from a rhombohedral-rich to a tetragonal-rich state. At this optimal composition, the material achieves a high piezoelectric coefficient ($d_{33} \approx 830$ pC/N) and an elevated Curie temperature ($T_c \approx 256$ °C), positioning it above the typical performance envelope of rare-earth-modified and conventional Pb-based ferroelectric systems. More importantly, the ceramic exhibits a high depolarization temperature ($T_d \approx 230$ °C), further highlighting its advantage for high-temperature applications and extending its practical operating range. Compared with commercial PZT-610HD, the designed ceramic offers a comparable room-temperature d_{33} but

a ≈70 °C higher T_d and a more temperature-insensitive response before depolarization. Atomic-resolution TEM reveals heterogeneous local polar configurations in the optimized composition, providing microscopic structural evidence consistent with the observed high piezoelectric response.

Full-matrix electromechanical characterization yields a complete and self-consistent set of elastic, dielectric, and piezoelectric constants. These data, together with the demonstrated thermal stability, provide a reliable engineering database for high-temperature piezoelectric actuators, sensors, and transducers. The strategy of combining rare-earth modification with high-T_c ternary solid solutions opens a viable route for further performance optimization in next-generation piezoceramics.

Acknowledgements

The authors are grateful for the scientific and technical support from Sydney Microscopy and Microanalysis (SMM). SMM is a Core Research Facility of the University of Sydney and a foundational node of Microscopy Australia (ROR: 042mm0k03) which is supported by the Australian Government's National Collaborative Research Infrastructure Scheme.

Funding

This work was supported by ONRG under grant number N62909-21-1-2037. X. Liao acknowledges financial support from the Australian Research Council Discovery Project DP190101155.

Author contributions

Conceptualization: S. Zhang, C. Gao; Methodology: S. Zhang, C. Gao; Sample preparation, property measurements, and formal analysis: C. Gao; TEM characterization and analysis: Y.

Liu, C. Gao, X. Liao; Experimental assistance: A. M. M. T. Karim and Y. Luo; Writing – original draft preparation: C. Gao; Writing – review and editing: S. Zhang, C. Gao; Supervision: S. Zhang. All authors discussed the results and approved the final manuscript.

Availability of data and materials

The data that support the findings of this study are available from the corresponding author upon reasonable request.

Competing interests

The authors have no competing interests to declare that are relevant to the content of this article.

Electronic Supplementary Material

Supplementary material including Rietveld refinement results, full-matrix measurement principles, parameter derivation procedures, consistency analyses, and additional dielectric, ferroelectric, and microstructural characterization is available in the online version of this article.

References

1. Damjanovic, D., Ferroelectric, dielectric and piezoelectric properties of ferroelectric thin films and ceramics. *Reports on progress in physics*, 1998. **61**(9): p. 1267.
2. Jaffe, W., *Cook, and H. Jaffe, Piezoelectric Ceramics*. 1971, Academic Press, New York.
3. Zhang, S., et al., Advantages and challenges of relaxor-$PbTiO_3$ ferroelectric crystals for electroacoustic transducers–A review. *Progress in materials science*, 2015. **68**: p. 1-66.
4. Rödel, J., et al., Perspective on the development of lead-free piezoceramics. *Journal of the American Ceramic Society*, 2009. **92**(6): p. 1153-1177.

5. Li, F., et al., Ultrahigh piezoelectricity in ferroelectric ceramics by design. *Nature materials*, 2018. **17**(4): p. 349-354.
6. Gao, B., et al., Unexpectedly high piezoelectric response in Sm-doped PZT ceramics beyond the morphotropic phase boundary region. *Journal of Alloys and Compounds*, 2020. **836**: p. 155474.
7. Bian, L., et al., Improved electromechanical properties of Pb ($Ni_{1/3}Nb_{2/3}$) O_3–$PbZrO_3$–$PbTiO_3$ ferroelectric ceramics via Sm-modification. *Ceramics International*, 2024. **50**(3): p. 5739-5745.
8. Luo, N., et al., PMN-PT based quaternary piezoceramics with enhanced piezoelectricity and temperature stability. *Applied Physics Letters*, 2014. **104**(18).
9. Luo, N., et al., New Pb ($Mg_{1/3}Nb_{2/3}$) O_3–Pb ($In_{1/2}Nb_{1/2}$) O3–$PbZrO_3$–$PbTiO_3$ quaternary ceramics: morphotropic phase boundary design and electrical properties. *ACS Applied Materials & Interfaces*, 2016. **8**(24): p. 15506-15517.
10. Jing, R., et al., Reversible phase transitions and enhanced electrostrain in BNST-xFN ceramics under electric and thermal stimuli. *Microstructures*, 2025. **5**(3): p. N/A-N/A.
11. Liu, Y., et al., Flexible polarization configuration in high-entropy piezoelectrics with high performance. *Acta Materialia*, 2022. **236**: p. 118115.
12. Jiao, Y., et al., Overview of high-entropy oxide ceramics. *Materials Today*, 2024. **77**: p. 92-117.
13. Rost, C.M., et al., Entropy-stabilized oxides. *Nature communications*, 2015. **6**(1): p. 8485.
14. Amiri, A. and R. Shahbazian-Yassar, Recent progress of high-entropy materials for energy storage and conversion. *Journal of Materials Chemistry A*, 2021. **9**(2): p. 782-823.
15. Karim, A.M.M.T., et al., Beyond MPB engineering: enhanced piezoelectricity and thermal stability assisted by high-entropy design. *Nature Communications*, 2026. **17**: p. 6596.
16. Wang, D., M. Cao, and S. Zhang, Phase diagram and properties of Pb ($In_{1/2}Nb_{1/2}$) O_3–Pb ($Mg_{1/3}Nb_{2/3}$) O_3–$PbTiO_3$ polycrystalline ceramics. *Journal of the European Ceramic Society*, 2012. **32**(2): p. 433-439.
17. Guo, Q., et al., Piezoelectric ceramics with high piezoelectricity and broad temperature usage range. *Journal of Materiomics*, 2021. **7**(4): p. 683-692.
18. Wang, D., M. Cao, and S. Zhang, Investigation of ternary system $PbHfO_3$–$PbTiO_3$–Pb ($Mg_{1/3}Nb_{2/3}$) O_3 with morphotropic phase boundary compositions. *Journal of the American Ceramic Society*, 2012. **95**(10): p. 3220-3228.

19. Wang, P., et al., Modified Pb ($Mg_{1/3}Nb_{2/3}$) O_3-$PbZrO_3$–$PbTiO_3$ ceramics with high piezoelectricity and temperature stability. *Journal of the American Ceramic Society*, 2021. **104**(10): p. 5127-5137.
20. Randall, C., et al., High performance, high temperature perovskite piezoelectric ceramics. *Piezoelectric Single Crystals and Their Applications*, 2004.
21. Hou, E., et al., Morphotropic region and piezoelectric properties of xPb ($In_{1/2}Nb_{1/2}$) O_3-(1-*x*) Pb ($Hf_{1-y}Ti_y$) O_3 ceramics. *Ceramics International*, 2020. **46**(17): p. 27394-27400.
22. Tang, H., et al., Piezoelectric property and strain behavior of Pb ($Yb_{1/2}Nb_{1/2}$) O_3–$PbHfO_3$–$PbTiO_3$ polycrystalline ceramics. *Journal of the American Ceramic Society*, 2013. **96**(9): p. 2857-2863.
23. Electrical, I.o. and E. Engineers, *ANSI/IEEE Std 176-1987: IEEE standard on piezoelectricity*. 1988: IEEE.
24. Zheng, F., et al., Sm-doped PIN-PMN-PT transparent ceramics with high curie temperature, good piezoelectricity, and excellent electro-optical properties. *ACS Applied Materials & Interfaces*, 2023. **15**(5): p. 7053-7062.
25. Wang, P., et al., Pb ($In_{1/2}Nb_{1/2}$) O_3-$PbZrO_3$-$PbTiO_3$ ternary ceramics with temperature-insensitive and superior piezoelectric property. *Journal of the European Ceramic Society*, 2022. **42**(9): p. 3848-3856.
26. Zhang, R., et al., High electric field-induced strain properties in La-doped Pb ($In_{1/2}Nb_{1/2}$) O_3–$PbZrO_3$–$PbTiO_3$ relaxor ferroelectric ceramics. *Ceramics International*, 2023. **49**(19): p. 31582-31590.
27. Hao, J., et al., Structure evolution and electrostrictive properties in $(Bi_{0.5}Na_{0.5})_{0.94}$ $Ba_{0.06}TiO_3$–M_2O_5 (M= Nb, Ta, Sb) lead-free piezoceramics. *Journal of the European Ceramic Society*, 2016. **36**(16): p. 4003-4014.
28. Liu, G., et al., Losses in ferroelectric materials. *Materials Science and Engineering: R: Reports*, 2015. **89**: p. 1-48.
29. Damjanovic, D. and M. Demartin, Contribution of the irreversible displacement of domain walls to the piezoelectric effect in barium titanate and lead zirconate titanate ceramics. *Journal of Physics: Condensed Matter*, 1997. **9**(23): p. 4943-4953.
30. Lin, D., et al., High rhombohedral to tetragonal phase transition temperature and electromechanical response in Pb ($Yb_{1/2}Nb_{1/2}$) O_3-Pb ($Sc_{1/2}Nb_{1/2}$) O_3-$PbTiO_3$ ferroelectric system near the morphotropic phase boundary. *Journal of the European Ceramic Society*, 2019. **39**(6): p. 2082-2090.

31. Zhang, Y., et al., Ultrahigh piezoelectric performance benefiting from quasi-isotropic local polarization distribution in complex lead-based perovskite. *Nano Energy*, 2022. **104**: p. 107910.
32. Cheng, M., et al., Improved piezoelectricity of lead-based PNN-PIN-PT ternary ceramics via polymorphic nanodomain modulation. *Journal of the European Ceramic Society*, 2023. **43**(12): p. 5231-5240.
33. Bian, L., et al., High-performance Pb ($Ni_{1/3}Nb_{2/3}$) O_3-$PbZrO_3$-$PbTiO_3$ ceramics with the triple point composition. *Journal of the European Ceramic Society*, 2021. **41**(14): p. 6983-6990.
34. Zhang, S., et al., Improving the piezoelectric properties of Pb (Ni, Nb) O_3-Pb (Hf, Ti) O_3 ceramics through Nd_2O_3 addition. *Journal of Alloys and Compounds*, 2023. **960**: p. 170778.
35. Jia, C.-L., et al., Direct observation of continuous electric dipole rotation in flux-closure domains in ferroelectric Pb (Zr, Ti) O_3. *Science*, 2011. **331**(6023): p. 1420-1423.
36. Jang, J. and S.-Y. Choi, Reduced dimensional ferroelectric domains and their characterization techniques. *Microstructures*, 2024. **4**(2): p. N/A-N/A.
37. Zhang, S. and F. Li, High performance ferroelectric relaxor-PbTiO3 single crystals: Status and perspective. *Journal of Applied Physics*, 2012. **111**(3).
38. Berlincourt, D. and H.H. Krueger, Domain processes in lead titanate zirconate and barium titanate ceramics. *Journal of Applied Physics*, 1959. **30**(11): p. 1804-1810.
39. Kungl, H., et al., Nonlinearity of strain and strain hysteresis in morphotropic LaSr-doped lead zirconate titanate under unipolar cycling with high electric fields. *Journal of applied physics*, 2007. **101**(4).
40. Damjanovic, D. and M. Demartin, The Rayleigh law in piezoelectric ceramics. *Journal of Physics D: Applied Physics*, 1996. **29**(7): p. 2057-2060.
41. Hall, D., et al., A high energy synchrotron x-ray study of crystallographic texture and lattice strain in soft lead zirconate titanate ceramics. *Journal of applied physics*, 2004. **96**(8): p. 4245-4252.
42. Saito, Y., et al., Lead-free piezoceramics. *Nature*, 2004. **432**(7013): p. 84-87.
43. Zhang, S., et al., Elastic, piezoelectric, and dielectric characterization of modified $BiScO_3$-$PbTiO_3$ ceramics. *ieee transactions on ultrasonics, ferroelectrics, and frequency control*, 2005. **52**(11): p. 2131-2139.